9754 *Inorg. Chem.* **2009**, *48*, 9754–9766
DOI: 10.1021/ic9011845

Inorganic Chemistry
Article

Electronic Structures of $[Ru^{II}(cyclam)(Et_2dtc)]^{+}$, $[Ru(cyclam)(tdt)]^{+}$, and $[Ru(cyclam)(tdt)]^{2+}$: An X-ray Absorption Spectroscopic and Computational Study (tdt = toluene-3,4-dithiolate; Et_2dtc = *N,N*-diethyldithiocarbamate(1-))

Carsten Milsmann,[†] Eckhard Bill,[†] Thomas Weyhermüller,[†] Serena DeBeer George,[‡] and Karl Wieghardt*,[†]

[†] *Max-Planck-Institut für Bioanorganische Chemie, Stiftstrasse 34-36, D-45470 Mülheim an der Ruhr, Germany, and*
[‡] *Department of Chemistry and Chemical Biology, Baker Laboratory, Cornell University, Ithaca, New York 14853*

Received June 19, 2009

The reaction of $[Ru^{III}(cyclam)Cl_2]Cl$ with 2 equiv of sodium *N,N*-diethyldithiocarbamate in methanol afforded $[Ru^{II}(cyclam)(Et_2dtc)](BPh_4)$ (**1**(BPh_4)). The same reaction with only 1 equiv of toluene-3,4-dithiol and a base yielded $[Ru(cyclam)(tdt)](PF_6)$ (**2**(PF_6)) which was oxidized by 1 equiv of ferrocenium hexafluorophosphate generating $[Ru(cyclam)(tdt)](PF_6)_2$ (**2**$^{ox}(PF_6)_2$). The crystal structures of **1** and **2** have been determined by X-ray crystallography at 100 K. The electronic structures of diamagnetic **1**(BPh_4), paramagnetic **2**(PF_6) ($S=^1/_2$), and diamagnetic **2**$^{ox}(PF_6)_2$ have been studied by magnetochemistry, spectroelectrochemistry, electron paramagnetic resonance spectroscopy, and ^{1}H NMR spectroscopy. X-ray absorption spectroscopy on Ru K- and L-edges as well as S K-edges has been employed. Finally, the molecular and electronic structures of all three species have been calculated by using density functional theory (B3LYP). It is shown that **2**^{ox} comprises an electronic structure which is best described by three resonance structures $\{[Ru^{II}(cyclam)(tdt^0)]^{2+} \leftrightarrow [Ru^{III}(cyclam)(tdt^{\bullet})]^{2+} \leftrightarrow [Ru^{IV}(cyclam)(tdt^{2-})]^{2+}\}$ with a closed-shell singlet ground state. This is in stark contrast to the isoelectronic iron species, namely, $[Fe^{III}(cyclam)(tdt^{\bullet})]^{2+}$ which is a singlet diradical with a low-spin ferric ion coupled intramolecularly antiferromagnetically to a ligand π radical monoanion $(tdt^{\bullet})^{-}$.

Introduction

In two recent articles we have shown that *S,S*′-coordinated benzene-1,2-dithiolate(1-) π radical monoanions, $(bdt^{\bullet})^{-}$, bound to a low-spin cobalt(III) ion,[1] a chromium(III) ion,[1] or a low-spin iron(III) ion[2] in complexes **A**, **B**, and **C**, respectively, represent a well-defined open-shell oxidation level of this ligand. In the corresponding monocations **A**′, **B**′, **C**′ this ligand is present in its reduced, closed-shell benzene-1,2-dithiolate(2-) form, $(bdt)^{2-}$ (Formula 1).[1,2]

$[Co^{III}(tren)(bdt^{\bullet})]^{2+}$	$[Cr^{III}(tren)(bdt^{\bullet})]^{2+}$	$[Fe^{III}(cyclam)(bdt^{\bullet})]^{2+}$
$S = {}^1/_2$	$S = 1$	$S = 0$
A	**B**	**C**

(1)

$[Co^{III}(tren)(bdt)]^{1+}$	$[Cr^{III}(tren)(bdt)]^{1+}$	$[Fe^{III}(cyclam)(bdt)]^{1+}$
$S = 0$	$S = {}^3/_2$	$S = {}^1/_2$
A'	**B'**	**C'**

It was shown that these π radical ligands in **A**, **B**, and **C** display spectroscopic properties very similar to those reported for corresponding complexes containing a benzosemiquinonate(1-) π radical[3,4] or a catecholate(2-) ligand in analogous monocations $[M(N_4)(cat)]^{1+}$ ($M = Co^{III}$, Cr^{III}).[4,5] This behavior is in part enforced by using the redox-stable LM^{III} moiety where L is a neutral, saturated tetradentate amine (e.g., tris(2-aminoethyl)amine (tren) and 1,4,8,11-tetraazacyclotetradecane (cyclam)) and M^{III} represents a low-spin Co^{III} ion, a Cr^{III} ion, or a low-spin Fe^{III} ion.

In contrast to this apparently straightforward description of the electronic structures, it has recently been shown by a number of groups that this is not the case for complexes of ruthenium. The discussion centers around the relative importance of the resonance structures shown in Scheme 1 of a given $[Ru(L)]^{1+/2+}$ moiety (where L represents a dioxolene, dithiolene, diimine-, aminophenolate-, or aminothiophenolate-type ligand).

For the monocationic Ru-dioxolene unit, a delocalized ground state with contributions from both $[Ru^{III}(L)^{2-}]^{+}$ and $[Ru^{II}(L^{\bullet})^{-}]^{+}$ forms has been proposed independently by Lever et al.[6] and Tanaka et al.,[7] while for the corresponding

*To whom correspondence should be addressed. E-mail: wieghardt@mpi-muelheim.mpg.de.

(1) Milsmann, C.; Bothe, E.; Bill, E.; Weyhermüller, T.; Wieghardt, K. *Inorg. Chem.* **2009**, *48*, 6211.
(2) Milsmann, C.; Patra, G. K.; Bill, E.; Weyhermüller, T.; DeBeer George, S.; Wieghardt, K. *Inorg. Chem.* **2009**, *48*, 7430.
(3) Wicklund, P. A.; Beckmann, L. S.; Brown, D. G. *Inorg. Chem.* **1976**, *15*, 1996.
(4) (a) Wheeler, D. E.; McCusker, J. K. *Inorg. Chem.* **1998**, *37*, 2296. (b) Rodriguez, J. H.; Wheeler, D. E.; McCusker, J. K. *J. Am. Chem. Soc.* **1998**, *120*, 12051.
(5) Wicklund, P. A.; Brown, D. G. *Inorg. Chem.* **1976**, *15*, 396.
(6) da Silva, R. S.; Gorelsky, S. I.; Dodsworth, E. S.; Tfouni, E.; Lever, A. B. P. *J. Chem. Soc., Dalton Trans.* **2000**, 4078.
(7) Wada, T.; Yamanaka, M.; Fujihara, T.; Miyazato, Y.; Tanaka, K. *Inorg. Chem.* **2006**, *45*, 8887.

Published on Web 09/21/2009

Scheme 1. Electronic Ground State Descriptions for an *o*-Quinoid Type Ligand Coordinated to Ru in Octahedral Geometry

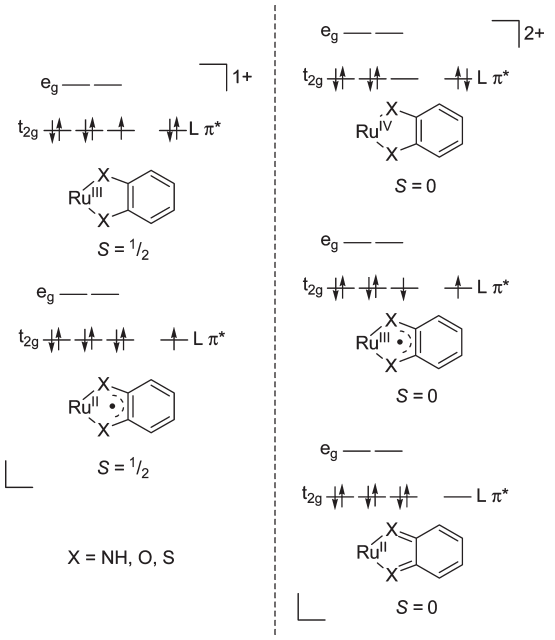

aminophenolate and aminothiophenolate complexes with two acetylacetonate, (acac), as spectator ligands, a $[Ru^{III}(L)^{2-}]^{+}$ formulation was suggested by Kaim and Lahiri.[8] However, for an aminophenolate complex containing two bipyridine, (bpy), ligands instead of acac, Kaim et al. proposed a $[Ru^{II}(L^{\bullet})]^{+}$ ground state with minor contributions of Ru to the singly occupied molecular orbital (SOMO) based on electron paramagnetic resonance (EPR) spectroscopy.[9] On the basis of structural parameters and density functional theory (DFT) calculations, Kaim et al.[8] and Lahiri et al.[10] suggested a $[Ru^{III}(L^{\bullet})]^{2+}$ description for the one-electron oxidized moiety in $[Ru(acac)_2(aminophenolate)]$, in which the ligand radical is antiferromagnetically coupled to the metal center. This ground state formulation has been extended to the corresponding 1,2-benzoquinone diimine type compounds by Lahiri et al., again supported by structural parameters and theoretical results.[10] The same electronic structure was suggested by us based on results for other transition metal complexes containing 1,2-benzoquinone diimine derived radical ligands.[11] In contrast, Lever et al. prefer a $[Ru^{II}(L)^{0}]^{2+}$ description with significant π-back bonding.[12]

Finally, a detailed theoretical investigation by Kaupp et al. suggested that the monocationic Ru-ligand moiety is better described as a superposition of the resonance structures $[Ru^{II}(L^{\bullet})^{-}]^{+}$ and $[Ru^{III}(L)^{2-}]^{+}$ for any *o*-quinonoid ligand.[13] This implies that the "true" spectroscopic oxidation state in these compounds is intermediate between the integer descriptions. Accordingly, the dicationic unit was described by the superposition of the $[Ru^{II}(L)^{0}]^{2+}$ and the $[Ru^{III}(L^{\bullet})^{-}]^{2+}$ resonance structures.[13] Thus, the strong delocalization of the valence electrons between the metal and the ligand could be a consequence of highly covalent interactions. This agrees well with calculations of nucleus-independent chemical shifts (NICS)[14] reported recently by Zarić et al.,[15] which showed that Ru-1,2-benzoquinone diimines exhibit metalloaromaticity.[16]

Scheme 2. Ligands and Complexes

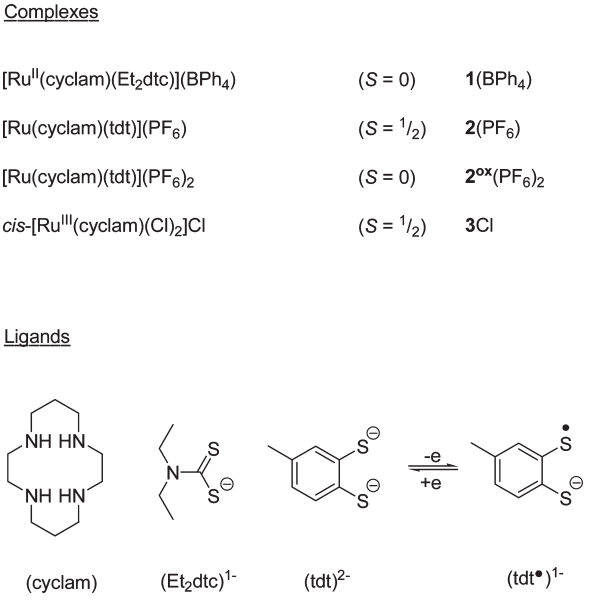

Here we report on the electronic structure of complexes **1**, **2**, and **2**^{ox} shown in Scheme 2. These complexes have been studied by X-ray crystallography, magnetic susceptibility measurements, spectroelectrochemistry, EPR, and X-ray absorption spectroscopy (S K-edge, Ru K- and L-edge). We have computationally corroborated these experimental results by DFT, including TD-DFT simulations of X-ray absorption and optical absorption spectra.

Experimental Section

Preparation of Complexes. The starting material *cis*-$[Ru^{III}(cyclam)Cl_2]Cl$ has been prepared as described in the literature.[17] The ligands are commercially available.

[Ru^{II}(cyclam)(Et$_2$dtc)](BPh$_4$) (1(BPh$_4$)). A solution of Na(Et$_2$dtc) (110 mg, 0.49 mmol) in degassed methanol (10 mL) was slowly added under strictly anaerobic conditions to a solution of *cis*-[Ru(cyclam)Cl$_2$]Cl (100 mg, 0.24 mmol) in degassed methanol/water (2:1, 25 mL). After stirring for 1 h, a solution of $NaBPh_4$ (103 mg, 0.3 mmol) in degassed methanol (2 mL) was added. A microcrystalline, yellow solid precipitated immediately, which was filtered in air quickly, washed subsequently with methanol/water (3: 1) and diethyl ether, and dried under vacuum. The product is air-stable for a few minutes in the

(8) Patra, S.; Sarkar, B.; Mobin, S. M.; Kaim, W.; Lahiri, G. K. *Inorg. Chem.* **2003**, *42*, 6469.
(9) Ye, S.; Sarkar, B.; Duboc, C.; Fiedler, J.; Kaim, W. *Inorg. Chem.* **2005**, *44*, 2843.
(10) Maji, S.; Patra, S.; Chakraborty, S.; Janardanan, D.; Mobin, S. M.; Sunoj, R. B.; Lahiri, G. K. *Eur. J. Inorg. Chem.* **2007**, 314.
(11) Bill, E.; Bothe, E.; Chaudhuri, P.; Chlopek, K.; Herebian, D.; Kokatam, S.; Ray, K.; Weyhermüller, T.; Neese, F.; Wieghardt, K. *Chem.—Eur. J.* **2005**, *11*, 204.
(12) (a) Rusanova, J.; Rusanov, E.; Gorelsky, S. I.; Christendat, D.; Popescu, R.; Farah, A. A.; Beaulac, R.; Reber, C.; Lever, A. B. P. *Inorg. Chem.* **2006**, *45*, 6246. (b) Kalinina, D.; Dares, C.; Kaluarachchi, H.; Potvin, P. G.; Lever, A. B. P. *Inorg. Chem.* **2008**, *47*, 10110.
(13) Remenyi, C.; Kaupp, M. *J. Am. Chem. Soc.* **2005**, *127*, 11399–11413.
(14) von Rague Schleyer, P.; Maerker, C.; Dransfeld, A.; Jiao, H.; van Eikema Hommes, N. J. R. *J. Am. Chem. Soc.* **1996**, *118*, 6317.
(15) Milcic, M. K.; Ostojic, B. D.; Zaric, S. D. *Inorg. Chem.* **2007**, *46*, 7109.
(16) Masui, H. *Coord. Chem. Rev.* **2001**, *219−221*, 957.
(17) Sakai, K.; Yamada, Y.; Tsubomura, T. *Inorg. Chem.* **1996**, *35*, 3163–3172.

solid state, but should be stored under an inert atmosphere. Yield: 137 mg (73%). Single crystals suitable for X-ray crystallography were grown from concentrated solutions of **1**(BPh_4) in CH_2Cl_2; Anal. Calcd for $C_{39}H_{54}BN_5RuS_2$: C 60.92, H 7.08, N 9.11; Found: C 61.15, H 7.12, N 9.10.

[Ru(cyclam)(tdt)](PF_6) (2(PF_6)). Under an Ar blanketing atmosphere a solution of H_2tdt (96 mg, 0.62 mmol) and potassium *tert*-butylate (150 mg, 1.34 mmol) in degassed methanol (10 mL) was added dropwise at 0 °C to a solution of *cis*-[Ru(cyclam)Cl_2]Cl (250 mg, 0.62 mmol) in degassed methanol/water (2:1, 50 mL). After stirring at 0 °C for 15 min, KPF_6 (130 mg, 0.7 mmol) was added, and the dark blue mixture was kept under argon at room temperature overnight with stirring. Upon evaporation of the solvent under a stream of argon dark red crystals were obtained. Yield: 254 mg (68%); ESI MS (pos. ions, CH_2Cl_2): *m*/*z*: 456 *cis*-[(cyclam)Ru(tdt)]$^+$; Anal. Calcd for $C_{17}H_{30}F_6N_4PRuS_2$: C 34.00, H 5.03, N 9.33; Found: C 34.10, H 4.97, N 9.35.

[Ru(cyclam)(tdt)](PF_6)$_2$ (2^{ox}(PF_6)$_2$). Solid ferrocenium hexafluorophosphate (55 mg, 0.17 mmol) was added to a solution of **2** (100 mg, 0.17 mmol) in dichloromethane (20 mL) under an argon blanketing atmosphere. After stirring for 1 h at room temperature, hexane (20 mL) was added. The dark pink precipitate was filtered, washed with pentane and dried under vacuum. Yield: 104 mg (84%); Anal. Calcd for $C_{17}H_{30}F_{12}N_4P_2RuS_6 \cdot H_2O$: C 26.74, H 4.22, N 7.34; Found: C 26.65, H 4.20, N 6.90.

X-ray Crystallographic Data Collection and Refinement of the Structures. An orange single crystal of **1**(BPh_4)·0.16CH_2Cl_2 and a dark blue crystal of **2**(PF_6) were coated with perfluoropolyether, picked up with nylon loops and mounted in the nitrogen cold stream of a Bruker-Nonius KappaCCD diffractometer equipped with a Mo-target rotating-anode X-ray source. Graphite monochromated Mo Kα radiation (λ = 0.71073 Å) was used throughout. Final cell constants were obtained from least-squares fits of several thousand strong reflections. Intensities of redundant reflection were used to correct for absorption using the program SADABS.[18] The structures were readily solved by Patterson methods and subsequent difference Fourier techniques. The Siemens ShelXTL software package[19] was used for solution and artwork of the structures, and ShelXL97[20] was used for the refinement. All non-hydrogen atoms were anisotropically refined, and hydrogen atoms were placed at calculated positions and refined as riding atoms with isotropic displacement parameters. Crystallographic data of the compounds are summarized in Table 1.

The macrocyclic ligand and the dithiocarbamate ligand in compound **1**(BPh_4)·0.16CH_2Cl_2 were found to be disordered, where the macrocycle is twisted by about 90°. A split atom model of the complex cation was refined yielding occupation ratios of almost 84:16. The SAME instruction of ShelXL97 was used to restrain the geometry of the split parts and equal anisotropic displacement parameters were refined for corresponding split atoms.

Severe disorder was also found for the PF_6^- anion in **2**(PF_6). Three split positions were refined with restrained bond distances and equal anisotropic displacement parameters for corresponding atoms, using the SAME and EADP instructions of ShelXL97.

Physical Measurements. Elemental analyses were measured at the Mikroanalytisches Labor H. Kolbe, in Mülheim an der Ruhr, Germany. Cyclic voltammograms and square wave voltammograms in the range of −25 to 25 °C were recorded by using an EG&G Potentiostat/Galvanostat 273A. A three electrode cell was employed with a glassy-carbon working electrode, a glassy-carbon auxiliary electrode, and a $Ag/AgNO_3$ reference electrode (0.01 M $AgNO_3$ in CH_3CN). Ferrocene was added as an internal standard after completion of the measurements and potentials are referenced versus the Fc^+/Fc couple. Controlled potential coulometric measurements were performed in a setup, which allows recording of absorption spectra in situ during electrolysis, by employing the same potentiostat, but using a Pt-grid as a working electrode. A Pt-brush was used as counter electrode and separated from the working electrode compartment by a Vycor frit. An $Ag/AgNO_3$ (0.01 M $AgNO_3$ in CH_3CN) reference electrode was employed again. UV−vis spectra were measured on a Hewlett-Packard 8452A diode array spectrophotometer (200−1100 nm) or a Perkin-Elmer UV−vis Lambda 19 spectrophotometer (250−2000 nm). Temperature-dependent magnetic susceptibilities were measured by using a SQUID magnetometer (MPMS Quantum Design) at 1.0 T (4−300 K). Underlying diamagnetism was corrected by using tabulated Pascal's constants. The susceptibility data were simulated using the program julX (by Eckhard Bill). X-band EPR derivative spectra were recorded on a Bruker ELEXSYS E500 spectrometer equipped with the Bruker standard cavity (ER4102ST) and a helium flow cryostat (Oxford Instruments ESR 910). Microwave frequencies were calibrated with a Hewlett-Packard frequency counter (HP5352B), and the field control was calibrated with a Bruker NMR field probe (ER035M). The spectra were simulated with the program GFIT (by Eckhard Bill) for the calculation of powder spectra with effective *g* values and anisotropic line widths (Gaussian line shapes were used).

X-ray Absorption Spectroscopy Measurements and Data Analysis. All data were measured at the Stanford Synchrotron Radiation Laboratory under ring conditions of 3.0 GeV and 60−100 mA. Ru K-edge XAS data were measured on a focused beamline 9−3. A Si(220) monochromator was utilized for energy selection. All samples were prepared as solids in boron nitride, pressed into a pellet, and sealed between 38 μm Kapton tape windows in a 1 mm aluminum spacer. The samples were maintained at 10 K during data collection using an Oxford Instruments CF1208 continuous flow liquid helium cryostat. Data were measured in transmission mode. Internal energy calibrations were performed by simultaneous measurement of

Table 1. Crystallographic Data for **1**(BPh_4)·0.16 CH_2Cl_2, and **2**(PF_6)

	1(BPh_4)·0.16 CH_2Cl_2	**2**(PF_6)
chem. formula	$C_{39.16}H_{54.32}BCl_{0.32}N_5RuS_2$	$C_{17}H_{30}F_6N_4PRuS_2$
crystal size, mm^3	0.04 × 0.03 × 0.01	0.06 × 0.04 × 0.02
fw	781.94	600.61
space group	$P2_1/n$, No. 14	*Cc*, No. 9
a, Å	17.669(3)	9.0606(5)
b, Å	12.777(2)	21.3736(12)
c, Å	17.816(3)	12.2031(5)
β, deg	109.305(3)	98.033(4)
V, Å^3	3795.9(11)	2340.0(2)
Z	4	4
T, K	100(2)	100(2)
ρ calcd, g cm^{-3}	1.368	1.705
refl. collected/$2\Theta_{max}$	107818/62.28	30284/62.00
unique refl./$I > 2\sigma(I)$	12168/9773	7438/6520
no. of params/restr.	575/75	326/66
λ, Å /μ(Kα), cm^{-1}	0.71073/5.80	0.71073/9.77
absolute structure param.		−0.01(2)
R1 [a]/goodness of fit [b]	0.0496 1.167	0.0356/ 1.048
wR2 [c] ($I > 2\sigma$ (I))	0.1183	0.0695
residual density, e Å^{-3}	+1.17/−0.94	+0.78/−0.60

[a] Observation criterion: $I > 2\sigma(I)$. $R1 = \sum||F_o| - |F_c||/\sum|F_o|$. [b] $GoF = [\sum[w(F_o^2 - F_c^2)^2]/(n - p)]^{1/2}$. [c] $wR2 = [\sum w(F_o^2 - F_c^2)^2/\sum w(F_o^2)^2]^{1/2}$ where $w = 1/\sigma^2(F_o^2) + (aP)^2 + bP$, $P = (F_o^2 + 2F_c^2)/3$.

(18) *SADABS, 2006/1*; Bruker AXS Inc.: Madison, WI, 2007.
(19) *ShelXTL 6.14*; Bruker AXS Inc.: Madison, WI, 2003.
(20) Sheldrick, G. M. *ShelXL97*; University of Göttingen: Göttingen, Germany, 1997.

the appropriate metal reference foil placed between a second and third ionization chamber. The first inflection point of a Ru metal foil was assigned to 22118.0 eV. Data represent two to three scan averages and were processed by fitting a second order polynomial to the pre-edge region and subtracting this background from the entire spectrum. A three-region cubic spline was used to model the smooth background above the edge. The data were normalized by subtracting the spline and normalizing the post-edge 1.0.

Ru L- and S K-edge data were measured using the 54-pole wiggler beamline 6−2 in high magnetic field mode of 10 kG with a Ni-coated harmonic rejection mirror and a fully tuned Si(111) double crystal monochromator. All data were measured at room temperature as fluorescence spectra. Samples were finely ground and dispersed on Mylar tape. To check for reproducibility, 2−3 scans were measured for each sample. The Ru L-edge energy was calibrated from Cl K-edge spectra of D_{2d}-$[CuCl_4]^{2-}$ run at intervals between sample scans. The maximum of the first pre-edge feature in the spectrum was fixed at 2820.20 eV. S K-edges were similarly calibrated using $Na_2S_2O_3$ as a reference, and assigning the maximum of the first pre-edge feature to 2472.02 eV. A step size of 0.08 eV was used over the edge region. Data were averaged, and a smooth background was removed from all spectra by fitting a polynomial to the pre-edge region and subtracting this polynomial from the entire spectrum. Normalization of the data was accomplished by fitting a flattened polynomial or straight line to the post-edge region and normalizing the post-edge to 1.0. Fits to the S K-edge spectra were performed using EDG_Fit.[21]

Calculations. All DFT calculations were performed with the ORCA[22] program package. The geometry optimizations of the complexes and single-point calculations on the optimized geometries were carried out using the B3LYP[23] functional. This hybrid functional often gives better results for transition metal compounds than pure gradient-corrected functionals, especially with regard to metal−ligand covalency.[24] The all-electron Gaussian basis sets were those developed by the Ahlrichs group.[25,26] Triple-ζ quality basis sets TZV(P) with one set of polarization functions on the metals and on the atoms directly coordinated to the metal center were used.[25] For the carbon and hydrogen atoms, slightly smaller polarized split-valence SV(P) basis sets were used, that were of double-ζ quality in the valence region and contained a polarizing set of d-functions on the non-hydrogen atoms.[26] Auxiliary basis sets used to expand the electron density in the resolution-of-the-identity (RI) approach were chosen,[27] where applicable, to match the orbital basis. The self-consistent field (SCF) calculations were tightly converged (1×10^{-8} E_h in energy, 1×10^{-7} E_h in the density change, and 1×10^{-7} in maximum element of the DIIS error vector). The geometry optimizations for all complexes were carried out in redundant internal coordinates without imposing symmetry constraints. In all cases the geometries were considered converged after the energy change was less than 5×10^{-6} E_h, the gradient norm and maximum gradient element were smaller than 1×10^{-4} E_h $Bohr^{-1}$ and 3×10^{-4} E_h $Bohr^{-1}$, respectively, and the root-mean square and maximum displacements of all atoms were smaller than 2×10^{-3} Bohr and 4×10^{-3} Bohr, respectively. Throughout this paper we describe our computational results by using the broken-symmetry (BS) approach by Ginsberg[28] and Noodleman.[29] Because several broken symmetry solutions to the spin-unrestricted Kohn−Sham equations may be obtained, the general notation BS(m,n)[30] has been adopted, where m(n) denotes the number of spin-up (spin-down) electrons at the two interacting fragments. Canonical and corresponding orbitals,[31] as well as spin density plots were generated with the program Molekel.[32] TD-DFT calculations were performed to predict the transitions in the pre-edge region of the S K-edge XAS spectra.[33] The symmetry equivalent sulfur 1s orbitals obtained from the ground state calculations were localized using the Pipek−Mezey criteria,[34] and TD-DFT calculations at the B3LYP level were performed, allowing only for excitations from the localized sulfur 1s orbitals. The basis sets were chosen to match the basis sets used for the single point ground state calculations. The obtained transition energies were corrected by a constant empirical shift of 56.3 eV to match the experimental spectra. TD-DFT calculations of the electronic absorption spectra were performed at the B3LYP level of theory. The conductor-like screening model (COSMO)[35] was applied to model the solvent effects of CH_2Cl_2.

Results and Discussion

(a). Synthesis and Characterization of Complexes. Complexes discussed and ligands used in the syntheses are summarized in Scheme 2. $[Ru^{II}(cyclam)(Et_2dtc)]^+$, **1**, was obtained by slow addition of 2 equiv of $NaEt_2dtc$ in methanol to a solution of *cis*-$[Ru^{III}(cyclam)Cl_2]Cl$ in methanol/water under strictly anaerobic conditions. In this reaction, Et_2dtc^- is not only a ligand, but also a reducing agent, which results in the formation of a Ru^{II} species and tetraethylthiuramdisulfide. Upon addition of $NaBPh_4$ in methanol to the reaction mixture, **1**(BPh_4) precipitated immediately as a bright yellow, air-sensitive solid (yield 73%). Single crystals suitable for X-ray crystallography were obtained by slow evaporation of concentrated solutions of **1**(BPh_4) in CH_2Cl_2/hexane yielding **1**(BPh_4)·0.16 CH_2Cl_2.

The complex $[Ru(cyclam)(tdt)]^+$, **2**, was isolated after the slow addition of H_2(tdt) in methanol to *cis*-$[Ru^{III}(cyclam)Cl_2]Cl$ in methanol/water in the presence of 2 equiv of KO^{t}Bu under anaerobic conditions ($(tdt)^{2-}$ represents toluene-3,4-dithiolate(2-)). An immediate color change from yellow to dark blue indicated the formation of **2**. Dark red crystals of **2**(PF_6) suitable for X-ray crystallography were isolated after addition of KPF_6 in water (yield 68%).

The one-electron oxidized complex $[Ru(cyclam)(tdt)]^{2+}$, $\mathbf{2^{ox}}$, was synthesized from **2** by using 1 equiv of ferrocenium hexafluorophosphate as oxidant. The reaction

(21) George, G. N. *EXAFSPAK & EDG_FIT*; Stanford Synchrotron Radiation Laboratory, Stanford Linear Accelerator Center, Stanford University: Stanford, CA, 2000.
(22) Neese, F. *Orca − an ab initio, DFT and Semiempirical Electronic Structure Package*, Version 2.6, Revision 35; Institut für Physikalische und Theoretische Chemie, Universität Bonn: Bonn, Germany, March 2008.
(23) (a) Becke, A. D. *J. Chem. Phys.* **1993**, *98*, 5648–5652. (b) Becke, A. D. *J. Chem. Phys.* **1986**, *84*, 4524. (c) Lee, C. T.; Yang, W. T.; Parr, R. G. *Phys. Rev. B* **1988**, *37*, 785.
(24) Neese, F.; Solomon, E. I. In *Magnetism: From Molecules to Materials*; Miller, J. S., Drillon, M., Eds.; Wiley: New York, 2002; Vol. *4*, p 345.
(25) Schäfer, A.; Huber, C.; Ahlrichs, R. *J. Chem. Phys.* **1994**, *100*, 5829.
(26) Schäfer, A.; Horn, H.; Ahlrichs, R. *J. Chem. Phys.* **1992**, *97*, 2571.
(27) (a) Eichkorn, K.; Weigend, F.; Treutler, O.; Ahlrichs, R. *Theor. Chem. Acc.* **1997**, *97*, 119–124. (b) Eichkorn, K.; Treutler, O.; Öhm, H.; Häser, M.; Ahlrichs, R. *Chem. Phys. Lett.* **1995**, *240*, 283. (c) Eichkorn, K.; Treutler, O.; Öhm, H.; Häser, M.; Ahlrichs, R. *Chem. Phys. Lett.* **1995**, *242*, 652.
(28) Ginsberg, A. P. *J. Am. Chem. Soc.* **1980**, *102*, 111.
(29) Noodleman, L.; Peng, C. Y.; Case, D. A.; Mouesca, J. M. *Coord. Chem. Rev.* **1995**, *144*, 199.
(30) Kirchner, B.; Wennmohs, F.; Ye, S.; Neese, F. *Curr. Opin. Chem. Biol.* **2007**, *11*, 134.
(31) Neese, F. *J. Phys. Chem. Solids* **2004**, *65*, 781–785.
(32) *Molekel*; Advanced Interactive 3D-Graphics for Molecular Sciences, available under http:\\www.cscs.ch/molkel/.
(33) DeBeer George, S.; Petrenko, T.; Neese, F. *Inorg. Chim. Acta* **2008**, *361*, 965.
(34) Pipek, J.; Mezey, P. G. *J. Chem. Phys.* **1989**, *90*, 4916.
(35) Klamt, A.; Schurmann, G. *J. Chem. Soc., Perkin Trans.* **1993**, *2*, 793.

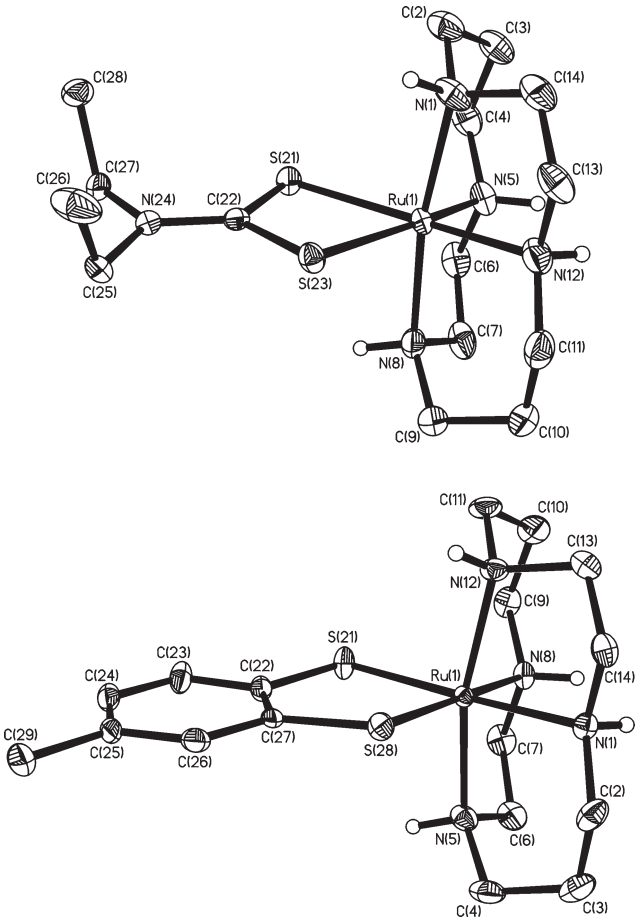

Figure 1. ORTEP representation of $\mathbf{1}(BPh_4)\cdot 0.16\ CH_2Cl_2$ at the 40% probability (top), and $\mathbf{2}(PF_6)$ (bottom) shown at the 40% probability level.

proceeded quickly in CH_2Cl_2 under an inert atmosphere with an immediate color change from dark blue to pink. Upon addition of hexane, the product $\mathbf{2}^{ox}(PF_6)_2$ precipitated as a dark pink powder (yield 84%).

(b). Crystal Structures. Single-crystal X-ray diffraction studies of $\mathbf{1}(BPh_4)\cdot 0.16\ CH_2Cl_2$ and $\mathbf{2}(PF_6)$ were performed at 100(2) K (Table 1). Structural representations of the two octahedral cations, **1** and **2**, are shown in Figure 1. Important bond lengths and angles are given in Table 2.

In the monocation **1**, the central ruthenium ion possesses a formal oxidation state of +II and a monoanionic, closed-shell dithiocarbamate ligand. The Ru−N bond lengths in **1** range from 2.101(7)−2.136(6) Å, which is in good agreement with known Ru^{II} amine complexes.[17,36,37] The Ru−S bond distances are long at 2.400(3) Å and 2.384(3) Å. The structural parameters of the dithiocarbamate ligand are in agreement with the parameters for the uncoordinated ligand[38] indicating that the ligand is indeed coordinated in its closed-shell monoanionic dithiocarbamato(1-) form.

Table 2. Selected Bond Distances (Å) and Folding Angles φ (deg) in **1** and **2**

1		**2**	
Ru(1)−N(1)	2.104(5)	Ru(1)−N(1)	2.133(3)
Ru(1)−N(5)	2.107(5)	Ru(1)−N(5)	2.163(3)
Ru(1)−N(12)	2.091(5)	Ru(1)−N(12)	2.174(3)
Ru(1)−N(8)	2.118 (4)	Ru(1)−N(8)	2.117(3)
Ru(1)−S(21)	2.3876(18)	Ru(1)−S(28)	2.3049(8)
Ru(1)−S(23)	2.3973(17)	Ru(1)−S(21)	2.2913(8)
S(21)−C(22)	1.717(5)	S(28)−C(27)	1.747(3)
S(23)−C(22)	1.724(5)	S(21)−C(22)	1.748(3)
C(22)−N(24)	1.341(6)	C(27)−C(26)	1.408(4)
		C(26)−C(25)	1.380(5)
		C(25)−C(24)	1.389(6)
		C(24)−C(23)	1.390(5)
		C(23)−C(22)	1.412(5)
		C(22)−C(27)	1.392(5)
		φ	6.83

For complex **2**, the total charge of +1 of the cation formally implies the presence of a Ru^{III} ion and a dianionic, closed-shell dithiolate(2-) ligand. However, the C−S bond lengths are observed at 1.748(3) Å. This value lies between the expected values for a closed-shell dianionic (1.77−1.76 Å) and a monoanionic radical (1.72−1.73 Å) dithiolene ligand.[39,40] On the other hand, the quinoidal distortion of the aromatic ring is not as pronounced as expected for a pure ligand radical. Thus, a clear identification of the oxidation state based on the structural parameters of the ligand is not possible. The Ru−N distances in the range of 2.133(3)−2.174(3) Å are rather long for Ru^{III} and therefore may support a Ru^{II} formulation for the central metal ion.[37] It is well established that the determination of the oxidation state of the central metal ion in Ru complexes based on bond distances alone is often ambiguous, since the differences in bond lengths between low-spin Ru^{II} and low-spin Ru^{III} are quite small.[37]

(c). Magnetochemistry and EPR Spectroscopy. Complex **1** is diamagnetic with an $S=0$ ground state. This is in agreement with a low-spin Ru^{II} (d^6) configuration.

Figure S1 shows the temperature-dependence of the effective magnetic moment, μ_{eff}, of $\mathbf{2}(PF_6)$ in the temperature range from 4 to 300 K in an applied field of 1.0 T. Above 80 K, the compound shows an almost temperature-independent μ_{eff} of 1.73 μ_B, which corresponds exactly to the expectation value for an $S={}^1/_2$ ground state. The data were readily simulated by including temperature-independent paramagnetism, χ_{TIP}, of 36.2×10^{-6} emu, a g_{av} value of 2.024, and a Weiss constant, θ, of −4.3 K. The small value for θ indicates only weak intermolecular antiferromagnetic coupling.

The X-band EPR spectrum of **2** in CH_2Cl_2 is shown in Figure S2. The spectrum exhibits significant hyperfine interactions with the N−H protons belonging to the cyclam ligand. This was proven by an H/D-exchange experiment. For this experiment, the EPR spectrum was initially recorded in frozen MeOH/toluene solution (toluene was added to improve the quality of the glass). In contrast to the spectrum in CH_2Cl_2, the resulting spectrum in MeOH shows no resolved hyperfine lines,

(36) (a) Chan, H.-L.; Liu, H.-Q.; Tzeng, B.-C.; You, Y.-A.; Peng, S.-M.; Yang, M.; Che, C.-M. *Inorg. Chem.* **2002**, *41*, 3161. (b) Chen, Y.-J.; Xie, P.; Heeg, M. J.; Endicott, J. F. *Inorg. Chem.* **2006**, *45*, 6282.
(37) Tfouni, E.; Ferreira, K. Q.; Doro, F. G.; da Silva, R. S.; da Rocha, Z. N. *Coord. Chem. Rev.* **2005**, *249*, 405–418.
(38) Mereiter, K.; Preisinger, A. *Inorg. Chim. Acta* **1985**, *98*, 71.
(39) Ray, K.; Weyhermüller, T.; Goossens, A.; Menno, W. J. C.; Wieghardt, K. *Inorg. Chem.* **2003**, *42*, 4082–4087.
(40) Ray, K.; Weyhermüller, T.; Neese, F.; Wieghardt, K. *Inorg. Chem.* **2005**, *44*, 5345–5360.

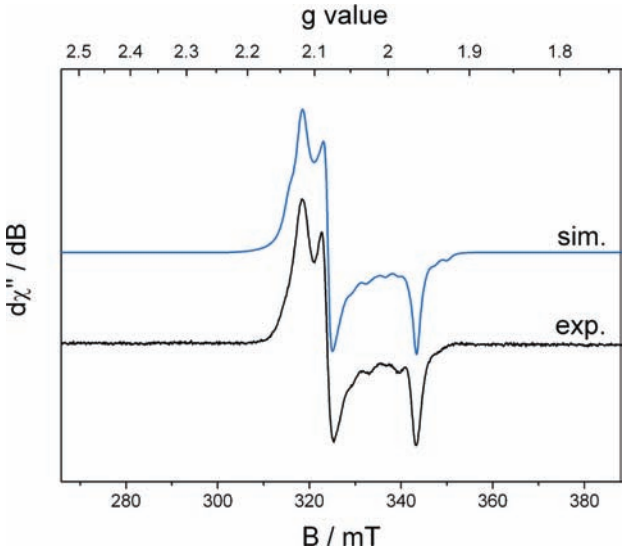

Figure 2. X-band EPR spectra of N-deuterated **2** recorded in frozen MeOD/toluene solution (0.2 mM, 10.0 K, frequency = 9.44 GHz, modulation = 1 mT, power = 0.1 mW).

but significant line broadening (Supporting Information, Figure S3). This can be attributed to hydrogen bonding between **2** and the polar, protic solvent MeOH. A dynamic hydrogen bonding network is present in solution. When this solution is rapidly frozen, the dynamic is quenched and a number of different conformations are present. When the experiment was conducted under the same conditions in d_1-MeOD, in the presence of catalytic amounts of sodium methoxide, the line broadening disappeared (Supporting Information, Figure S3). Under these experimental conditions, only the N−H protons can be exchanged. Unfortunately, even with this additional information, the spectrum including proton hyperfine coupling (Supporting Information, Figure S2) could not be simulated successfully. Although the correct number of peaks was obtained assuming two equivalent protons (one above and one below the dithiolene plane) the intensities could not be reproduced. This is most likely due to the presence of multiple conformations of the complex in frozen solution, resulting in complicated line shape patterns.

Instead, the experimental spectrum of *N*-deuterated **2** was simulated (Figure 2). The spectrum displays a rhombic signal with $g_x = 2.119$, $g_y = 2.082$, $g_z = 1.964$ ($g_{av} = 2.055$). Interestingly, the observed *g*-anisotropy of **2** is significantly smaller than that reported for $[Fe^{III}(cyclam)(tdt)]^+$ in ref 2 ($g_x = 2.291$, $g_y = 2.176$, $g_z = 1.958$). This suggests a significant ligand π radical contribution $[Ru^{II}(cyclam)(tdt^{\bullet})]^{1+}$ to the SOMO of **2** but not a full π radical as in $[Co^{III}(tren)(bdt^{\bullet})]^{2+}$ ($S = {}^1/_2$) with $g_x = 2.036$, $g_y = 2.018$, $g_z = 2.000$ described in ref 1. This notion is also supported by the hyperfine coupling of the unpaired electron to the ^{99}Ru and ^{101}Ru nuclei (both $I = {}^5/_2$), which have a natural abundance of 12.7% and 17.0%, respectively. For the simulation, both isotopes were treated with identical hyperfine coupling constants, owing to their very similar nuclear properties. The best fit of the data was achieved using $^{99/101}$Ru hyperfine coupling constants of $A_{xx} = 8.0$ G, $A_{yy} = 30.0$ G, $A_{zz} = 24.5$ G ($A_{av} = 20.8$ G). The hyperfine splitting indicates that the unpaired electron in **2** resides in an orbital with significant metal contribution. Thus, it is not possible at this point to unambiguously assign a spectroscopic oxidation state for both the metal and the dithiolene ligand in **2** based on EPR spectroscopy. In fact, the above results suggest a delocalized ground state description with significant contributions from $[Ru^{II}(cyclam)(tdt^{\bullet})]^+$ as well as $[Ru^{III}(cyclam)(tdt^{2-})]^+$.

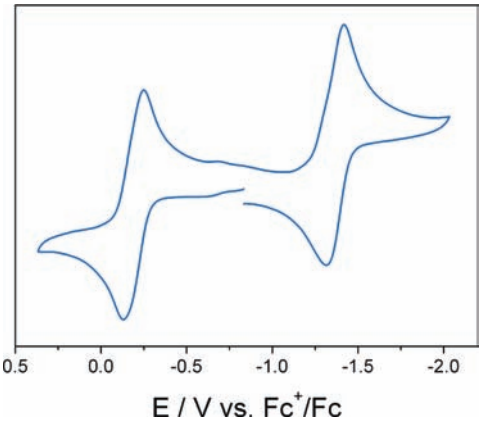

Figure 3. Cyclic voltammogram of **2** in CH_2Cl_2 at room temperature (0.10 M $[N(n\text{-}Bu)_4]PF_6$, scan rate 200 mV s^{-1}, glassy carbon working electrode).

(d). Spectroelectrochemistry. The cyclic voltammogram of **2** in CH_2Cl_2 containing 0.10 M $[N(n\text{-}Bu)_4]PF_6$ as the supporting electrolyte using a glassy carbon working electrode is shown in Figure 3. The redox potentials are referenced against the ferrocenium/ferrocene couple (Fc^+/Fc). The electrochemical properties are very similar to those of the corresponding iron complex $[Fe^{III}(cyclam)(tdt)]^+$ in ref 2. Controlled-potential coulometry established that the two observable electron transfer waves represent reversible one-electron redox processes. The redox couple at −1.37 V corresponds to a reduction of **2**, yielding the neutral complex $\mathbf{2^{red}}$. The second redox couple at −0.18 V is due to a reversible oxidation of **2** resulting in the one-electron oxidized, dicationic species $\mathbf{2^{ox}}$. Compared to the corresponding iron complex the entire cyclic voltammogram is shifted to lower potentials, while the separation of the two redox processes remains almost identical (~1.2 V).

The electronic absorption spectrum of **2** in CH_2Cl_2 is shown in Figure 4. The visible region of the spectrum is dominated by two intense charge transfer (CT) bands at 706 nm ($\varepsilon = 4400$ M^{-1} cm^{-1}) and 537 nm ($\varepsilon = 1390$ M^{-1} cm^{-1}). This is very similar to the spectrum of the analogous iron species. However, the peaks are shifted to higher energy and show much larger intensities. Since the intensity of CT bands is strongly dependent on the overlap of the donor and acceptor orbitals,[41,42] this indicates stronger covalency and consequently stronger delocalization of the orbitals in **2** as compared to the corresponding iron species. This behavior agrees nicely with the results from EPR spectroscopy.

(41) Lever, A. B. P.; Gorelsky, S. I. *Struct. Bonding* (*Berlin*) **2004**, *107*, 77.
(42) Lever, A. B. P.; Dodsworth, E. S. In *Inorganic Electronic Structure and Spectroscopy*; Solomon, E. I., Lever, A. B. P., Eds.; Wiley: New York, 1999; Vol. *2*, p 227.

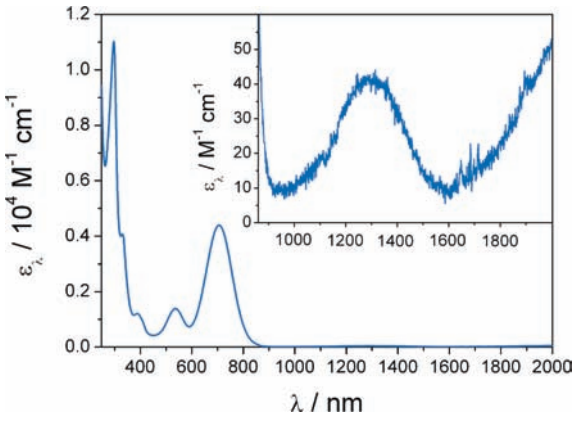

Figure 4. Electronic absorption spectrum of **2** in CH_2Cl_2 at room temperature.

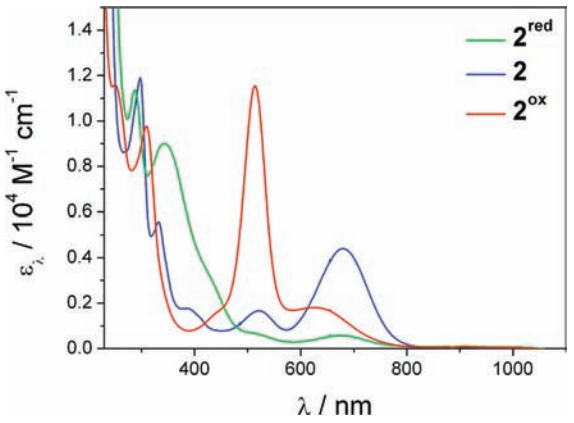

Figure 5. Electronic absorption spectra of **2** (blue) and its electrochemically generated oxidized and reduced form, $\mathbf{2}^{ox}$ (red) and $\mathbf{2}^{red}$ (green), respectively, in CH_2Cl_2 at −25 °C.

Additionally, two very low intensity bands with extinction coefficients $\varepsilon_\lambda < 100\ M^{-1}\ cm^{-1}$ are observed in the near-infrared region (NIR). These bands are not observed in the spectrum of the iron analogue. The lower of the two bands has its maximum at 1290 nm, while the maximum of the second band lies outside of the experimentally accessible region. Thus, neither the intensity nor the exact peak position of this low energy transition was determined. A detailed analysis of the absorption spectrum of **2** will be provided in the DFT section (vide infra).

The spectral changes observed in the region between 250 and 1100 nm upon electrochemical oxidation to the dication $\mathbf{2}^{ox}$ and upon reduction yielding the neutral compound $\mathbf{2}^{red}$ are shown in Figure 5. The reduction to $\mathbf{2}^{red}$ was not driven to completeness and no NIR data was obtained because of the low stability of this species under the conditions of the coulometric experiment. Upon reduction to $\mathbf{2}^{red}$, the CT bands of **2** disappear. This is to be expected, since $\mathbf{2}^{red}$ is $[Ru^{II}(cyclam)(tdt)]^0$, in which both the ligand π^*-orbital and the Ru t_{2g} orbitals are completely filled and, therefore, no charge transfer transitions are possible.

The spectrum of the one-electron oxidized complex $\mathbf{2}^{ox}$ is dominated by a very intense charge-transfer transition at 527 nm ($\varepsilon = 11540\ M^{-1}\ cm^{-1}$). Weaker bands in the visible region are found at 439 nm ($\varepsilon = 1740\ M^{-1}\ cm^{-1}$) and 631 nm ($\varepsilon = 2350\ M^{-1}\ cm^{-1}$). The width of the latter peak indicates that it is composed of at least two electronic transitions. Interestingly, the analysis of the NIR region (Supporting Information, Figure S4) reveals an additional feature around 1300 nm, which shows only very low intensity ($\varepsilon \sim 200\ M^{-1}\ cm^{-1}$).

(e). X-ray Absorption Spectroscopy. The Ru K-edge spectra of **1**, **2**, $\mathbf{2}^{ox}$ and *cis*-$[Ru^{III}(cyclam)Cl_2]^+$, **3**, are shown in Figure 6. The rising edge energies determined at the first inflection point are summarized in Table 3. The complexes **1** and **3** can be considered as reference compounds for genuine Ru^{II} and Ru^{III} species, respectively. As expected, the rising edge energy for **1** is 1.2 eV lower than for **3** corresponding to a change in oxidation state of one unit. For **2**, the rising edge energy was determined to be 22115.3 eV, which lies between the boundaries set by the reference compounds **1** and **3**. This is in perfect agreement with the result obtained by EPR spectroscopy that the electronic ground state of **2** is best described by an equal contribution of the resonance structures $[Ru^{II}(cyclam)(tdt^{\bullet})]^+$ and $[Ru^{III}(cyclam)(tdt)]^+$. Finally, $\mathbf{2}^{ox}$ shows a rising edge energy of 22115.6 eV, which suggests a spectroscopic oxidation state of +III.

For ruthenium, L-edge XAS has proven to be a useful tool in the assignment of electronic structures. The Ru L_{II} and L_{III} edges are dominated by the dipole-allowed 2p → 4d transitions. Their energies vary depending on the electronic structure of the central metal ion.[43] Changes in the effective nuclear charge, because of a change in oxidation state or coordination number, affect the energy of the 2p and 4d orbitals, whereas changes in the ligand field only affect the energy of the 4d orbitals.

The Ru L_{II}-edge spectra of **1**, **2**, $\mathbf{2}^{ox}$, and **3** are shown in Figure 6, and the edge energies determined at the point of maximum absorption intensity are summarized in Table 3. The spectrum of the Ru^{II} species **1** shows only a single edge feature at 2969.7 eV. This arises because of a transition from the 2p orbital to the e_g set within the d orbital manifold, since the t_{2g} set is completely filled for a low spin d^6 system. In contrast, **3** shows an additional shoulder around 2969 eV which can be attributed to a transition into the t_{2g} set, which exhibits an electron hole because of the higher oxidation state of +III (d^5) for the metal. The e_g transition is found at 2970.7 eV for **3**, which corresponds to a one unit change in the oxidation state of the ruthenium compared to **1**. Complex **2** also shows two L_{II}-edge transitions, which confirms that the ground state cannot be adequately described as $[Ru^{II}(cyclam)(tdt^{\bullet})]^+$. Similar to the K-edge data, the L_{II}-edge energy shows that the oxidation state of **2** lies between +II and +III, since the e_g transition is found at 2970.3 eV. This is significantly different from both **1** (Ru^{II}) and **3** (Ru^{III}). The L_{II}-edge spectrum of $\mathbf{2}^{ox}$ shows two edge features and an e_g transition at 2970.6 eV in agreement with a Ru^{III} description. The intensity of the t_{2g} peak increases slightly from **2** to $\mathbf{2}^{ox}$, indicating more hole character in the t_{2g} set for $\mathbf{2}^{ox}$. The difference in the edge energies between **2** and $\mathbf{2}^{ox}$ is consistently 0.3 eV in both the Ru K-edge and Ru

(43) (a) Cramer, S. P.; deGroot, F. M. F.; Ma, Y.; Chen, C. T.; Sette, F.; Kipke, C. A.; Eichhorn, D. M.; Chan, M. K.; Armstrong, W. H. *J. Am. Chem. Soc.* **1991**, *113*, 7937. (b) George, S. J.; Lowery, M. D.; Solomon, E. I.; Cramer, S. P. *J. Am. Chem. Soc.* **1993**, *115*, 2968. (c) Wasinger, E. C.; de Groot, F. M. F.; Hedman, B.; Hodgson, K. O.; Solomon, E. I. *J. Am. Chem. Soc.* **2003**, *125*, 12894.

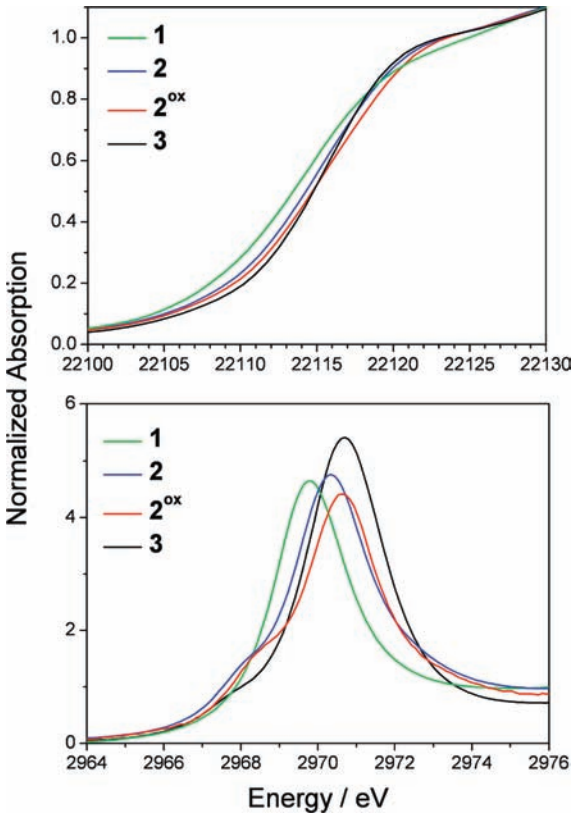

Figure 6. Normalized Ru K-edge (top) and Ru L_{II}-edge (bottom) X-ray absorption spectra of **1** (green), **2** (blue), $\mathbf{2^{ox}}$ (red), and $[Ru^{III}(cyclam)(Cl)_2]Cl$, **3** (black).

Table 3. Ru Edge Energies of Complexes **1**−**3**[a]

	1	**2**	$\mathbf{2^{ox}}$	**3**
K-edge energy/eV	22114.6	22115.3	22115.6	22115.8
L_{II}-edge energy/eV	2969.7	2970.3	2970.6	2970.7

[a] The K-edge energies are determined at the first inflection point of the rising edge. L_{II}-edge energies are determined at the maximum of the absorption curve.

L_{II}-edge XAS. While this establishes that the ruthenium center is affected by the oxidation, it does not account for a full one unit change of the oxidation state at the metal center.

A comparison of the S K-edge spectra of **2** and $\mathbf{2^{ox}}$ is shown in Figure 7. The intense low-energy pre-edge feature at 2470.0 eV for **2** can be assigned to a transition from the S 1s orbital into the SOMO of the doublet species. This feature already indicates a high radical character of the dithiolene ligand in agreement with significant contributions of the $[Ru^{II}(cyclam)(tdt^{\bullet})]^+$ resonance structure. Compared to the corresponding iron species the intensity of the peak is significantly higher (0.9 in **2** vs 0.6 in the iron complex), which can be attributed to a higher sulfur contribution to the SOMO because of stronger π-delocalization. On the other hand, the very broad feature at 2472.7 eV can be assigned to transitions to the σ-antibonding e_g orbitals, which show some multiplet splitting. The pseudo-Voigt fit of the spectrum of **2**, shown in Figure S5, shows very clearly that this feature consists of two transitions (shown in blue). This can only be explained by a significant

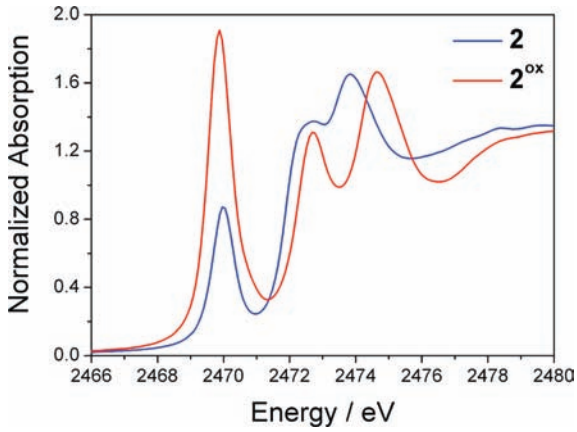

Figure 7. Comparison of the normalized S K-edge spectra of **2** (blue) and $\mathbf{2^{ox}}$ (red).

contribution of the $[Ru^{III}(cyclam)(tdt^{2-})]^+$ resonance structure, in which the unpaired electron resides in a metal orbital. However, the magnitude of the multiplet splitting in **2** is only ~0.5 eV, which is half of the magnitude found for the isoelectronic iron complex. Since multiplet effects are a direct consequence of unpaired spin density,[44] this suggests that the spin density on the metal is lower for **2** than for the iron analogue. In summary, this confirms that the unpaired electron is delocalized over metal and ligand in **2**, and that both resonance structures (containing either Ru^{II} or Ru^{III}) contribute to the ground state. The larger splitting between the d_{xz}/radical peak (shown in red in Figure S5) and the e_g transitions (blue) for **2** compared to the iron complex is expected for a second-row transition metal and has been observed previously for a series of bis-dithiolene complexes containing Ni, Pd, and Pt.[45]

The deconvoluted S K-edge spectrum of $\mathbf{2^{ox}}$ is shown in Figure S6. The spectrum shows very similar features to those observed for **2**. This suggests that the overall orbital manifold of the complexes is very similar. However, three major differences are apparent. First, the low-energy pre-edge transition at 2469.9 eV (shown in red) exhibits a much higher intensity than that observed in **2**. This indicates that upon oxidation, the electron is removed from the SOMO, without dramatically changing the composition of the orbital. Since the SOMO in **2** is delocalized over metal and ligand by a strong covalent π-interaction, the oxidation creates a delocalized LUMO in $\mathbf{2^{ox}}$. This situation is best described by resonance structures $\{[Ru^{II}(cyclam)(tdt^0)]^{2+} \leftrightarrow [Ru^{III}(cyclam)(tdt^{\bullet})]^{2+} \leftrightarrow [Ru^{IV}(cyclam)(tdt^{2-})]^{2+}\}$. Note that in the case of equal contributions, the effective average oxidation state for the Ru ion in $\mathbf{2^{ox}}$ is +III, which is in agreement with the results from Ru K- and L-edge XAS. This is in stark contrast to the oxidation of $[Fe^{III}(cyclam)(tdt)]^+$ to the corresponding dication,[2] where the electron is not removed from the metal centered SOMO, but from the closed-shell ligand, resulting in an

(44) (a) Fadley, C. S.; Shirley, D. A.; Freeman, A. J.; Bagus, P. S.; Mallow, J. V. *Phys. Rev. Lett.* **1969**, *23*, 1397. (b) de Groot, F. *Coord. Chem. Rev.* **2005**, *249*, 31.

(45) Ray, K.; DeBeer George, S.; Solomon, E. I.; Wieghardt, K.; Neese, F. *Chem.—Eur. J.* **2007**, *13*, 2783.

Table 4. Calculated and Experimental Bond Distances

	6			7		7
	exp.	calc.		exp.	calc.	calc.
Ru(1)−N(1)	2.104(5)	2.181	Ru(1)−N(1)	2.133(3)	2.188	2.195
Ru(1)−N(5)	2.107(5)	2.199	Ru(1)−N(5)	2.163(3)	2.239	2.236
Ru(1)−N(12)	2.091(5)	2.200	Ru(1)−N(12)	2.174(3)	2.240	2.236
Ru(1)−N(8)	2.118 (4)	2.181	Ru(1)−N(8)	2.117(3)	2.188	2.196
Ru(1)−S(21)	2.3876(18)	2.469	Ru(1)−S(28)	2.3049(8)	2.366	2.333
Ru(1)−S(23)	2.3973(17)	2.469	Ru(1)−S(21)	2.2913(8)	2.365	2.333
S(21)−C(22)	1.717(5)	1.743	S(28)−C(27)	1.747(3)	1.757	1.715
S(23)−C(22)	1.724(5)	1.743	S(21)−C(22)	1.748(3)	1.757	1.715
C(22)−N(24)	1.341(6)	1.337	C(27)−C(26)	1.408(4)	1.415	1.423
			C(26)−C(25)	1.380(5)	1.387	1.378
			C(25)−C(24)	1.389(6)	1.412	1.430
			C(24)−C(23)	1.390(5)	1.387	1.378
			C(23)−C(22)	1.412(5)	1.415	1.423
			C(22)−C(27)	1.392(5)	1.415	1.447
			φ	6.83	0.23	0.32

antiferromagnetically coupled singlet diradical. Second, the transitions to the σ-antibonding e_g orbitals (blue) show no multiplet splitting, which is further evidence for a closed-shell singlet ground state. Third, the electric dipole-allowed S K-edge feature shifts from 2473.9 eV in **2** to 2474.6 eV in $\mathbf{2^{ox}}$, indicating that the oxidation is affecting the oxidation level of the ligand.

(f). DFT Calculations. Geometry optimizations and electronic ground state calculations for **1**, **2**, and $\mathbf{2^{ox}}$ were performed at the B3LYP level of DFT, and the obtained structural parameters are summarized in Table 4. With the exception of the typical overestimation of the metal−ligand bond lengths, the optimized structures for **1** and **2** are in excellent agreement with the X-ray crystallographically determined parameters. For **1**, a diamagnetic ($S = 0$) ground state was assumed for the calculations, resulting in a spin-restricted closed-shell singlet solution. The calculated electronic structure also confirms the low-spin Ru^{II} oxidation state assignment, with three doubly occupied Ru d orbitals of almost equal energy (t_{2g} set) and two empty metal d orbitals (e_g set).

The calculated average C−S bond length of 1.76 Å for **2** corresponds to the arithmetic average of calculated C−S bond distances at 1.79 Å for $[Co^{III}(tren)(bdt)]^+$ and $[Cr^{III}(tren)(bdt)]^+$ containing a closed-shell dianionic dithiolene and at 1.73 Å for the corresponding dications containing a pure dithiolene π radical. The quinoidal distortion of the phenyl ring is also intermediate between closed-shell and ligand radical. This suggests a delocalized ground state with the two resonance structures $\{[Ru^{II}(cyclam)(tdt^{\bullet})]^+ \leftrightarrow [Ru^{III}(cyclam)(tdt^{2-})]^+\}$, effectively yielding a "half-radical" ligand and a ruthenium ion in the oxidation state of "+2.5". In this situation, the oxidation state formalism is not an applicable concept. This is nicely supported by the Mulliken spin-population analysis, which is shown in Figure 8. The unpaired electron is localized to ~40 % on the ruthenium ion, while the remaining spin density is found on the ligand. As has been shown previously[40] the spin density in a dithiolene radical is localized mainly on the sulfur atoms, which in the case of **2** carry a total spin density of 46 %.

The MO diagram shown in Figure 8 emphasizes that the unpaired electron resides in an orbital that is a linear combination of the Ru d_{xz} and a ligand π^*-orbital. The MO is π-antibonding with respect to the metal−ligand

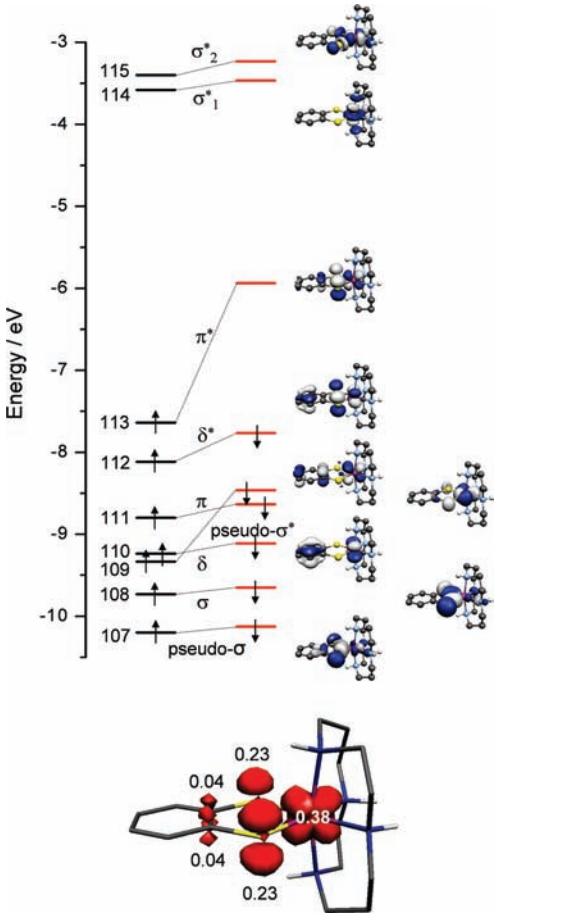

Figure 8. Top: Kohn−Sham MOs and energy scheme for **2** from spin-unrestricted B3LYP DFT calculations. The labels indicate the type of interaction between metal and ligand. Bottom: Mulliken spin density plot for **2**. α-spin density is shown in red.

interaction. The metal d_{xz} character in the empty 113 β orbital, representing the electron hole of the SOMO in the doublet species, is 34.9% (Table 5). The discrepancy between the orbital composition of the SOMO and the spin density population is due to spin polarization of the doubly filled MOs. Spin polarization has been shown to be an important factor for the interpretation of electronic structures and the assignment of oxidation states.[13]

In contrast to the isoelectronic, diamagnetic iron compound $[Fe^{III}(cyclam)(tdt^{\bullet})]^{2+}$, which was shown to be a singlet diradical species by broken symmetry (BS) DFT calculations, no reasonable BS solution was found for $\mathbf{2^{ox}}$. The energy difference between the BS(1,1) solution and the simple closed-shell singlet ($S=0$) solution is very small (0.6 kcal mol^{-1}). Furthermore, for BS(1,1) no spin density is found on the ruthenium ion, but the two S atoms carry spin density of opposite sign (0.34 spins each). Instead, the best description for the electronic ground state of $\mathbf{2^{ox}}$ is that of a closed-shell singlet representing a delocalized ground state as described by the resonance structures $\{[Ru^{II}(cyclam)(tdt^0)]^{2+} \leftrightarrow [Ru^{III}(cyclam)(tdt^{\bullet})]^{2+} \leftrightarrow [Ru^{IV}(cyclam)(tdt^{2-})]^{2+}\}$.

The calculated C−S bond lengths for $\mathbf{2^{ox}}$ of 1.72 Å are remarkably short, which is even shorter than the calculated values for the radical species $[Co^{III}(tren)(bdt^{\bullet})]^{2+}$, $[Cr^{III}(tren)(bdt^{\bullet})]^{2+}$, and $[Fe(cyclam)(bdt^{\bullet})]^{2+}$. This implies a significant contribution of the $[Ru^{II}(cyclam)(tdt^0)]^{2+}$

Table 5. Composition of Selected One-Electron Molecular Orbitals of **2** (%) As Obtained from the B3LYP DFT Calculations

		Ru					S		Ph	N	other
		d_{xz}	d_{yz}	$d_{x^2-y^2}$	d_{xy}	d_{z^2}	$p_{x/y}$	p_z			
					Unoccupied MOs						
115	β				56.3		21.8		1.6	10.5	9.8
	α				55.9		22.4		1.7	10.8	9.2
114	β					46.0	3.8		0.8	20.4	29.0
	α					53.7	4.4		0.7	20.7	20.5
113	β	34.9						38.4	18.2	2.8	5.7
					Occupied MOs						
	α	16.8						44.5	31.8	2.4	4.5
112	β		29.3					40.4	27.7	0.2	2.4
	α		33.4					33.4	30.0	0.2	3.0
111	β	47.1						7.4	39.1	2.0	4.4
	α			69.2			16.9		4.5	2.0	7.4
110	β			70.9			16.0		3.9	1.8	7.4
	α		45.5					0.8	44.8	0.6	8.3
109	β		49.0					1.0	43.8	0.8	5.4
	α	54.9							36.4	4.2	4.5
108	β				10.9		66.6		2.0	10.8	9.7
	α				10.8		66.1		2.2	12.0	8.9
107	β			17.9			47.4		12.3	8.0	14.4
	α			20.0			47.4		10.3	8.8	13.5

Table 6. Composition of Selected Two-Electron Molecular Orbitals of $\mathbf{2^{ox}}$ (%) As Obtained from the B3LYP DFT Calculations

	Ru					S		Ph	N	other
	d_{xz}	d_{yz}	$d_{x^2-y^2}$	d_{xy}	d_{z^2}	$p_{x/y}$	p_z			
				Unoccupied MOs						
115				55.7		20.8		2.2	12.2	9.1
114					59.6	4.2		1.0	25.0	10.2
113	27.1						40.0	21.2	3.4	8.3
				Occupied MOs						
112		29.0					32.6	36.4	0.2	7.8
111			65.9			18.6		4.9	2.7	7.9
110	44.3						1.6	42.1	4.4	7.6
109		50.1					0.6	43.4	1.0	4.9
108				4.5		56.8		2.6	19.9	16.2
107			18.5			29.8		9.0	18.7	24.0

resonance structure, where $(tdt)^0$ is the neutral, diamagnetic 1,2-dithiosemiquinone form of the $(tdt)^{2-}$ reduced form. In fact, the analysis of the MO diagram (Figure 9) shows that the LUMO (113) of $\mathbf{2^{ox}}$ is an antibonding linear combination of the Ru d_{xz} and a ligand π^*-orbital, similar to the SOMO of **2**, but with a decreased metal contribution of 27.1% (Table 6). Conversely, the corresponding bonding linear combination (110) has a much higher metal contribution (44.3%), so that the overall electron count for ruthenium lies somewhere in between a d^5 (Ru^{III}) and d^6 (Ru^{II}) configuration.

(g). TD-DFT Calculations. TD-DFT calculations of the S K-edge spectra were conducted for **2** and $\mathbf{2^{ox}}$ at the B3LYP level of theory, following the methodology described in ref 2. A comparison of the calculated and experimental spectra is shown in Figure 10. The pre-edge features in the spectrum of **2** are reproduced with excellent agreement in intensity and relative peak position. The lowest energy peak is due to a transition of a S 1s β-electron into the delocalized SOMO (113 β, $d_{xz}+L_{\pi^*}$),

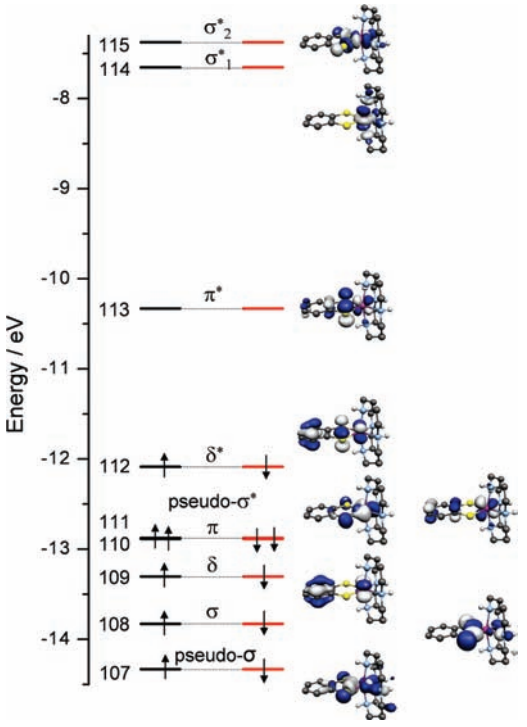

Figure 9. Kohn−Sham MOs and energy scheme for $\mathbf{2^{ox}}$ from spin-restricted B3LYP DFT calculations. The labels indicate the type of interaction between metal and ligand.

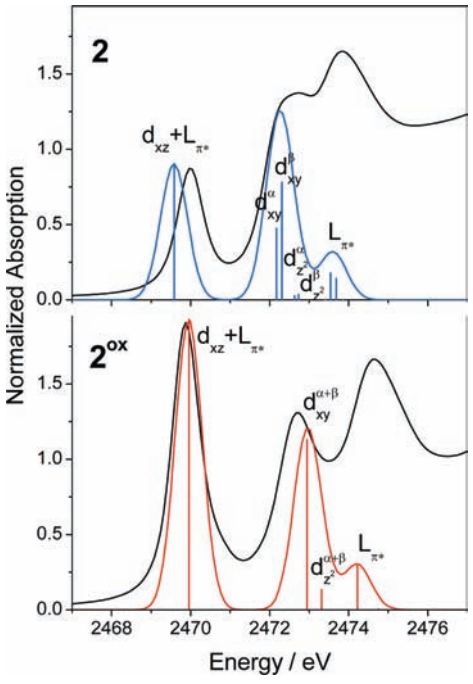

Figure 10. Comparison of the calculated (blue and red) and experimental (black) S K-edge XAS spectra of **2** (top) and $\mathbf{2^{ox}}$ (bottom). The calculated transitions are represented by the stick plots.

and its transition energy was calculated to be 2469.9 eV. The relatively high intensity is attributed to a high sulfur contribution to the SOMO (38.4%) because of strong π-delocalization. The subsequent four transitions are due to transitions into the d_{xy} and d_{z^2} orbitals (115 and 114), respectively. Similar to the corresponding transitions in $[Fe^{III}(cyclam)(tdt)]^+$ these are further split into an α- and

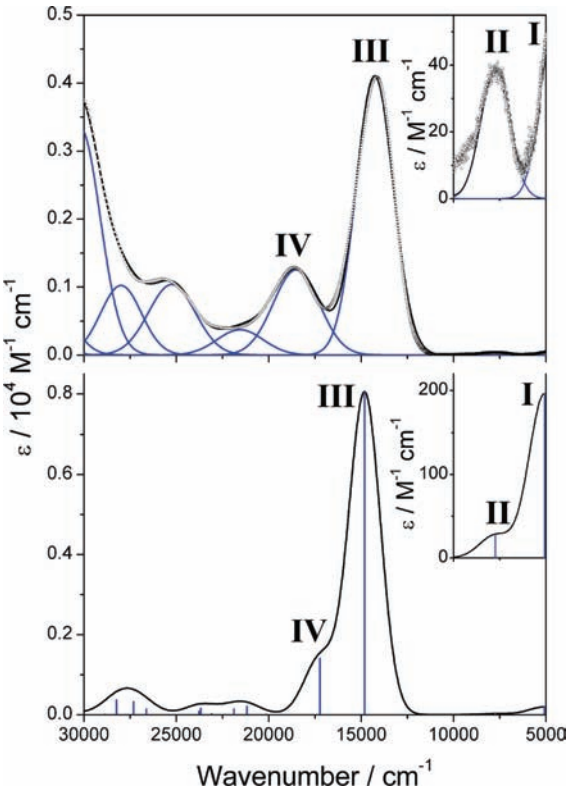

Figure 11. Top: Results from the Gaussian deconvolution of the experimental spectrum of **2** between 30000 and 5000 cm^{-1}. The Roman numerals indicate the main transitions discussed in the text. Bottom: TD-DFT (COSMO) calculated electronic absorption spectrum of **2** (B3LYP). The vertical bars indicate the position of the calculated transitions.

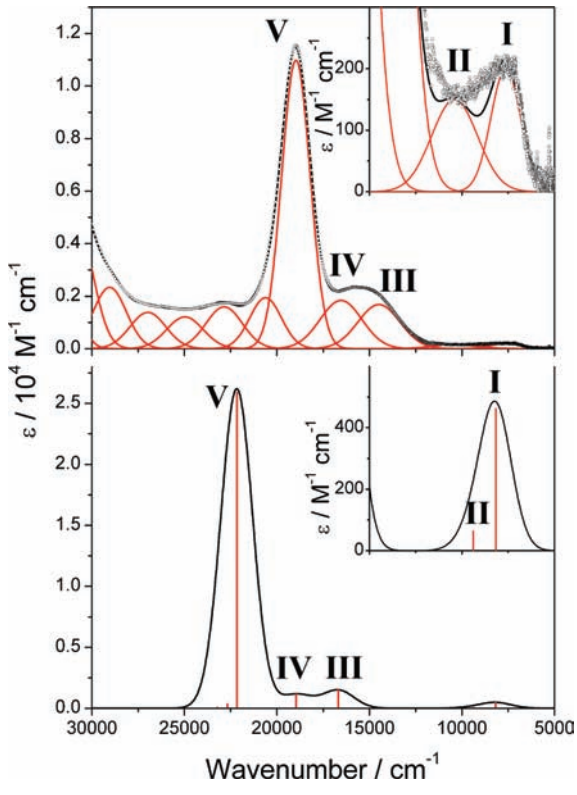

Figure 12. Top: Results from the Gaussian deconvolution of the experimental spectrum of $\mathbf{2^{ox}}$ between 30000 and 5000 cm^{-1}. The Roman numerals indicate the main transitions discussed in the text. Bottom: TD-DFT (COSMO) calculated electronic absorption spectrum of $\mathbf{2^{ox}}$ (B3LYP). The vertical bars indicate the position of the calculated transitions.

a β-transition by spin polarization, which is a crude estimate for the multiplet effects arising from the final-state configuration.[2,46] The magnitude of the splitting is predicted to be ~0.1 eV, which is significantly underestimated, compared to the experimental result. However, the decrease in the multiplet splitting observed in **2** compared to that in the iron analogue is nicely reproduced. The smaller splitting observed in **2** is most likely due to the higher delocalization of the unpaired electron density.

The S K-edge spectrum of $\mathbf{2^{ox}}$ was also successfully reproduced (Figure 10). In agreement with the closed-shell singlet ground state and in contrast to the corresponding open-shell singlet iron species $[Fe^{III}(cyclam)(tdt^{\bullet})]^{2+}$, no multiplet splitting is calculated for the transitions to the d_{xy} and d_{z^2} orbitals (acceptor orbitals 115 and 114, respectively). The spectrum is dominated by the very intense transition to the LUMO (orbital 113, 27.1% Ru d_{xz}, 40.0% S). Thus, the careful analysis of the calculated transitions confirms that the orbital manifold remains in principle unchanged. The independent reproduction of the spectral features of **2** and $\mathbf{2^{ox}}$ is an excellent indication for the validity of the calculated electronic structures.

To predict the electronic absorption spectra of **2** and $\mathbf{2^{ox}}$, TD-DFT calculations were performed at the B3LYP level of theory based on the electronic ground states described above. COSMO[35] was applied to model the solvent effects of CH_2Cl_2 used in the experiment. The experimental oscillator strength, f, of a transition can be calculated from the absorption spectrum by using eq 2:

$$f_{0\rightarrow I} = \frac{4.32 \times 10^{-9}}{n} \int_{\text{Band}} \varepsilon^{(I)}(\tilde{\nu})\, \mathrm{d}\tilde{\nu} \qquad (2)$$

where $f_{0\rightarrow I}$ is the oscillator strength of the transition from the ground state to the I^{th} electronic excited state, n is the refractive index of the solvent (1.4242 for CH_2Cl_2), $\varepsilon^{(I)}$ represents the extinction coefficient, and $\tilde{\nu}$ is the transition energy of the absorption maxima in cm^{-1}.[42] The integral term corresponds to the area under the absorption band. To obtain these values, the experimental spectra were subjected to Gaussian deconvolution. The Gaussian deconvolution spectra and the TD-DFT predicted spectra of **2** and $\mathbf{2^{ox}}$ are shown in Figure 11 and Figure 12, respectively. Gratifyingly, the experimental spectra are very well reproduced by the calculations. The most characteristic bands are found below 20000 cm^{-1} and are labeled with Roman numerals. A comparison between the experimental and calculated values for these bands is summarized in Table 7.

The assignment of the bands was deduced from the calculation. Although electronic transitions are multielectron processes, all multielectron states in the present examples are composed of one major one-electron transition, which contributes over 80% to the transition. Therefore, a single-electron transition can be assumed for a simplified approach. For all four transitions in **2**, the acceptor orbital is the strongly delocalized SOMO

(46) Berry, J. F.; DeBeer George, S.; Neese, F. *Phys. Chem. Chem. Phys.* **2008**, *10*, 4361.

Table 7. Analysis of the Visible and NIR Transitions of **2** and $\mathbf{2^{ox}}$ Following Gaussian Deconvolution of the Experimental Data, Combined with the Results Obtained from TD-DFT (COSMO) Calculations at the B3LYP Level

		energy, cm^{-1} (nm)		oscillator strength (*f*)		
	transition	expt.[a]	calcd.	expt.	calcd.	assignment
2	**I**		5076 (1970)		0.0018	112 $\beta \rightarrow$ 113β
	II	7800 (1284)	7749 (1291)	0.0003	0.0003	110 $\beta \rightarrow$ 113 β
	III	14300 (701)	14816 w675)	0.0336	0.0740	111 $\beta \rightarrow$ 113 β
	IV	18600 (537)	17236 580)	0.0124	0.0130	109 $\beta \rightarrow$ 113 β
$\mathbf{2^{ox}}$	**I**	7500 (1330)	8170 (1224)	0.0011	0.0043	112 $\rightarrow$ 113
	II	10200 (980)	9386 (1066)	0.0016	0.0006	111 $\rightarrow$ 113
	III	14500 (688)	16682 (599)	0.0150	0.0137	109 $\rightarrow$ 113
	IV	16800 (597)	18959 (528)	0.0180	0.0104	108 $\rightarrow$ 113
	V	19000 (528)	22165 (451)	0.0594	0.2385	110 $\rightarrow$ 113

[a] $\pm 100\ cm^{-1}$.

(113 β, see Table 5), which contains major contributions from ruthenium (34.9% d_{xz}) and the dithiolene ligand (56.6% π^*) and is π-antibonding with respect to the interaction between metal and ligand (M−L π^*). The acceptor orbital for the five main transitions in $\mathbf{2^{ox}}$ is the LUMO (113 see Table 6), which is qualitatively similar to the SOMO of **2**. Only the contributions from Ru d_{xz} (27.1%) and dithiolene π^* (61.2%) are slightly different. The most intense transition in both complexes is the result of an excitation from the M−L π-bonding equivalent of the acceptor orbital and can, therefore, formally be considered as a simple $\pi-\pi^*$ transition. Reassuringly, the calculations even reproduce the very weak transitions **I** and **II** in the near-IR region of the spectra.

Overall the excellent agreement between the calculated and the experimental electronic absorption spectra of **2** and $\mathbf{2^{ox}}$ confirms the electronic structures obtained from DFT calculations.

Conclusions

The present study allows a detailed comparison of the electronic structures of three isoelectronic species, namely, $[Co^{III}(tren)(bdt^{\bullet})]^{2+}$ ($S = {}^1/_2$),[1] $[Fe^{III}(cyclam)(tdt)]^{+}$ ($S = {}^1/_2$),[2] and $[Ru(cyclam)(tdt)]^{+}$ ($S = {}^1/_2$). Despite the fact that all three complexes exhibit a doublet ground state, their electronic structures differ significantly: While $[Co^{III}(tren)(bdt^{\bullet})]^{2+}$ has been shown by EPR spectroscopy and DFT calculations to consist of an almost pure *S*,*S*′-coordinated ligand π radical $(bdt^{\bullet})^{-}$ and a low-spin Co(III) ion (d^6; $S_{Co} = 0$),[1] no evidence for an electronic structure as $[Co^{IV}(tren)(bdt)]^{2+}$ has been found with a low-spin Co(IV) ion ($S_{Co} = {}^1/_2$). A corresponding electronic structure has been identified in $[Fe^{III}(cyclam)(tdt)]^{+}$ where a low-spin ferric ion ($S_{Fe} = {}^1/_2$) and a closed-shell *S*,*S*′-coordinated toluene-3,4-dithiolate(2-) ligand have been identified by EPR, S K-edge XAS, and DFT calculations.[2] The complex $[Ru(cyclam)(tdt)]^{+}$ possesses an electronic structure which is intermediate between the two extremes, namely, a ligand centered π radical in the cobalt complex and a metal-centered SOMO in the corresponding iron species. DFT calculations nicely corroborate the notion that the SOMO is shifted from predominantly ligand centered in $[Co^{III}(tren)(bdt^{\bullet})]^{2+}$ to metal-centered in $[Fe^{III}(cyclam)(tdt^{2-})]^{+}$ via the delocalized configuration represented by two resonance structures $\{[Ru^{II}(cyclam)(tdt^{\bullet})]^{+} \leftrightarrow [Ru^{III}(cyclam)(tdt^{2-})]^{+}\}$.

This behavior is clearly a consequence of the energies of the metal d orbitals which depend on their respective nuclear charges, Z_{eff}, which increase with the formal oxidation state (e.g., $Co^{III} \rightarrow Co^{IV}$; $Ru^{II} \rightarrow Ru^{III}$). Assuming identical charges, Z_{eff} increases from left to right in the transition metal series and from first row to second row transition metal ions. Schematically we can construct the bonding scheme shown in Figure 13:

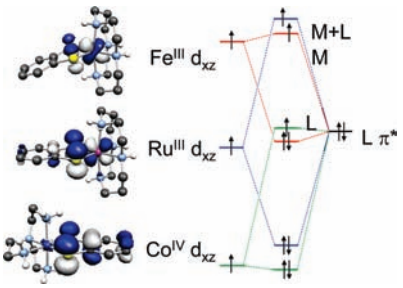

Figure 13. Simplified bonding scheme for the π interactions in $[Fe^{III}(cyclam)(tdt)]^{1+}$, $[Ru(cyclam)(tdt)]^{1+}$, and $[Co^{III}(tren)(bdt^{\bullet})]^{2+}$.

For $Fe^{III}(cyclam)(tdt^{2-})]^{+}$ the energy of the metal d orbitals is higher than the ligand π donor orbitals giving rise to a "normal" bonding situation with a metal centered SOMO (d_{xz}) located at a low-spin ferric ion. The corresponding cobalt complex $[Co^{III}(tren)(bdt^{\bullet})]^{2+}$ exhibits the lowest d orbital energies due to the presumed higher formal oxidation state of a Co(IV) low-spin d^5 fragment. The metal orbitals are significantly lower in energy than the ligand π orbital which results in an "inverted" bonding situation. As a consequence one electron is transferred from the ligand to the metal ion affording a ligand π radical, $(bdt^{\bullet})^{-}$, and a low-spin Co(III) ion. For the ruthenium species the metal d orbitals are lower in energy than for the iron species but higher than for Co(IV). Consequently, the d_{xz} orbital can form a highly covalent π bond with the ligand π donor orbital. The resulting SOMO is now shared between the Ru ion and the ligand. The assignment of an integer physical oxidation state is no longer meaningful, and the two resonance structures as shown above are more realistic.

A comparison of the electronic structures of the two isoelectronic oxidized species $[Fe^{III}(cyclam)(tdt^{\bullet})]^{2+}$ ($S = 0$) and $[Ru(cyclam)(tdt^{\bullet})]^{2+}$ ($S = 0$) demonstrates again subtle differences. Whereas the dicationic iron species has been clearly identified as a singlet diradical where a low-spin ferric ion ($S_{Fe} = {}^1/_2$; d^5) is intramolecularly antiferromagnetically coupled to a ligand π radical monoanion, $(tdt^{\bullet})^{-}$, ($S_{rad} = {}^1/_2$) the corresponding ruthenium species is better described as a closed-shell singlet ($S = 0$). The S K-edge spectrum of $\mathbf{2^{ox}}$

reveals a covalent bonding situation. Therefore, this closed-shell singlet ground state can be represented by the three resonance structures $\{[Ru^{II}(cyclam)(tdt^{0})]^{2+} \leftrightarrow [Ru^{III}(cyclam)(tdt^{\bullet})]^{2+} \leftrightarrow [Ru^{IV}(cyclam)(tdt^{2-})]^{2+}\}$.

This work demonstrates the fascinating differences in the electronic structures of three (formally) isoelectronic and "isostructural" complexes and their manifestations on the spectroscopic and structural properties. However, subtle changes in the electronic structures can only be successfully unveiled by a comprehensive combination of different spectroscopic and computational methods.

Acknowledgment. We are grateful for financial support from the Fonds der Chemischen Industrie. C.M. thanks the Max-Planck Society for a stipend. The Structural Molecular Biology program is supported by the National Institutes of Health (Grant 5 P41 RR001209), National Center for Research Resources, Biomedical Technology Program, and by the Department of Energy, Office of Biological and Environmental Research.

Supporting Information Available: X-ray crystallographic files in CIF format of **1** and **2**. Figure S1 shows the temperature dependence of the magnetic moment of **2**; Figure S2 shows the X-band EPR spectrum of **2** in frozen CH_2Cl_2 solution at 30 K; Figure S3 displays the X-band EPR spectrum of **2** in frozen MeOH/toluene solution and d_1-MeOH/toluene solution at 30 K; Figure S4 shows the electronic absorption spectrum of $\mathbf{2^{ox}}$ in CH_2Cl_2 solution at room temperature; Figure S5 shows pseudo-Voigt fits to the S K-edge XAS data of **2**, and Figure S6 those of $\mathbf{2^{ox}}$. This material is available free of charge via the Internet at http://pubs.acs.org.